World Scientific
www.worldscientific.com

Optical design and simulation of an integrated OCT and video rigid laryngoscope

Jiajing Kang*, Xinyu Li*, Mingming Wan*, Jiahui Wang†,
Shanshan Liang*,§ and Jun Zhang*,‡,¶

*School of Electronic and Information Technology
Sun Yat-sen University, Guangzhou 510006, P. R. China

†School of Physics, Sun Yat-Sen University
Guangzhou 510006, P. R. China

‡School of Artificial Intelligence
Guilin University of Electronic Technology
Guilin 541004, P. R. China
§liangshsh@mail.sysu.edu.cn
¶junzhang@guet.edu.cn

An integrated optical coherence tomography (OCT) and video rigid laryngoscope have been designed to acquire surface and subsurface tissue images of larynx simultaneously. The dual-modality system that is based on a common-path design with components as few as possible effectively maintains the light transmittance without compromising the imaging quality. In this paper, the field of view (FOV) of the system can reach 70° by use of a gradient index (GRIN) lens as the relay element and a four-lens group as the distal objective, respectively. The simulation showed that the modulation transfer function (MTF) value in each FOV of the rigid video endoscope at 160 lp/mm is greater than 0.1 while the root mean square (RMS) radii of the OCT beam in the center and edge of the FOV are 14.948 μm and 73.609 μm, respectively. The resolutions of both OCT and video endoscope meet the requirement of clinical application. In addition, all the components of the system are spherical, therefore the system can be of low cost and easy to assemble.

Keywords: Rigid endoscope; optical coherence tomography; integrated laryngoscope.

1. Introduction

Larynx is the transportation hub of human body and plays an important role in speech, deglutition, respiration and so on. Laryngeal tissue lesions will cause great inconvenience to patients, and even lead to their death. In order to early diagnose laryngeal diseases and to perform the re-evaluation of larynx after surgical treatment of lesions, noninvasive/ minimally invasive diagnostic techniques are of

§,¶Corresponding authors.

great interest. In clinical practice, the diagnosis of laryngeal pathology is usually performed using vocal test and endoscope to assess changes in morphology and function of the laryngeal tissue.[1] With the help of a video endoscope, doctors can better detect the lesions by observing the laryngeal tissue directly and make diagnostic decisions. However, the video endoscope can only provide images of superficial tissue and cannot image deep tissue. A biopsy is usually performed to determine the pathological state of tissue, which is the golden standard for cancer diagnosis. However, a large number of false negatives may be caused due to sampling errors. More importantly, biopsy is invasive and can cause scar, which would damage the quality of the sound.[2]

As a noninvasive, high resolution, cross-sectional imaging technique[3] capable of acquiring two-dimensional cross-sectional and three-dimensional volumetric images of tissue samples, OCT has been used in many fields of clinical applications.[4–6] Conventional video endoscopes provide a quick preview of the examined tissue, while OCT enables real-time 3D imaging by capturing the depth information of tissues. Therefore, the integration of OCT and video endoscope has the potential to increase the accuracy of diagnosis. Sergeev *et al.* first integrated OCT with a commercial endoscope to visualize the structure of tissue.[7] The OCT and endoscope channels placed parallelly were wrapped in a housing to form a unitary probe to collect images of mucous membranes. Guo *et al.* combined an OCT imaging system with a rigid video endoscope to build a two-channel laryngeal diagnostic imaging system.[8,9] Using a commercial rigid endoscope and a GRIN lens-based OCT imaging probe, the whole device was cumbersome and difficult to operate in the larynx region. In 2015, Alxander

et al. from the Hannover Laser Center integrated an OCT imaging system with a rigid endoscope to build a single-channel endoscope. With this design, the size of the device was greatly reduced.[10] However, the relay part of the system consisting of 12 lenses was a complex design and caused a one-way power loss of 15.5% resulting in a poor image quality.

In this paper we designed and simulated an integrated OCT and video rigid laryngoscope using optical design software Zemax. Only one GRIN lens was used as the relay lens and the distal objective contained only four lenses. The OCT and video endoscope shared the same relay system and distal end objective. Since a few lenses were used, the transmittance of the OCT signal reached more than 90%. In addition, the optimization of video endoscope was performed to achieve high-definition imaging quality. Under the criterion that the modulation transfer function is greater than 0.1, the resolution of the video endoscope system at each FOV is above 160 lp/mm. The spot size at the central FOV of OCT system was within the diffraction limit and the spot size at the edge of the FOV was closed to diffraction limit. With the benefits of low power loss and high imaging quality, the compact integration of OCT system and video endoscope could synchronously acquire the depth and superfical information of laryngeal tissue, which could provide an accurate diagnosis for the clinical application and an advanced methodology for pathological exploration.

2. Design Parameters of the Integrated Laryngoscope

Figure 1 shows the schematic of an integrated laryngoscope consisting of dual imaging modalities
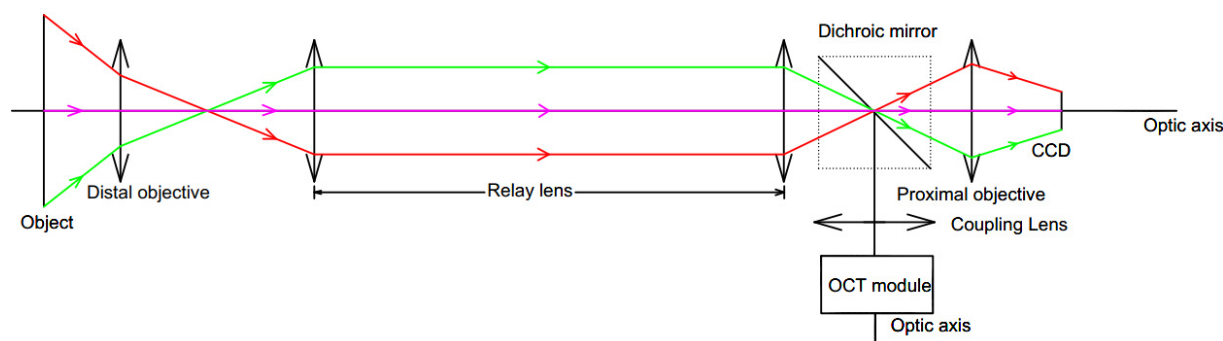

Fig. 1.   Schematic of the integrated laryngoscope.

of OCT and video endoscope. In this design, a dichroic mirror was inserted after the relay lens in the endoscope, from which the light of OCT module was coupled into the endoscope. Therefore, the video endoscope and OCT can be integrated into one single channel by sharing the relay lens and the distal objective. This design ensures that both modalities simultaneously image the same region, which is of great significance to early and accurate diagnosis.

For a video endoscope, it usually consists of three parts: the distal objective, the relay system and the proximal objective.[11] The relay system mainly functions as an image transmission system and the proximal objective is used to couple the image to the charge-coupled device (CCD). To fulfil the clinical requirements, we set the FOV and the diameter of the endoscope to 70° and 6 mm, respectively. The imaging size and the resolution of the optical system were determined by the dimension and pixel size of the CCD. Here, a 1/8″ CCD sensor (1280 ∗ 1024 pixels, pixel size 5.3 μm × 5.3 μm) was selected and the entrance pupil diameter was set to be 0.5 mm. Therefore, the focal length and f/# (the ratio of the effective focal length over the entrance pupil diameter) of the distal objective can be calculated to be 3.875 mm and 7.75 mm respectively according to Eq. (1)[12]:

$$y' = -f' \tan \omega, \tag{1}$$

where y' is the half height of image, ω is the half FOV and f' is the focal length on image side, respectively.

The cutoff frequency of the system can be calculated to be[13]:

$$\begin{aligned} \text{Resolution} &= 1/(2 \times \text{pixel size of CCD}) \\ &= 94 \, \text{lp/mm.} \end{aligned} \tag{2}$$

In other words, an MTF value of the video endoscope should be greater than 0.1 at a resolution of 94 lp/mm (MTF > 94 lp/mm@0.1).

The design indexes of the video endoscope are summarized in Table 1:

The FOV of an optical imaging system is determined by the position and the dimension of the stop used in the system. In our integrated laryngoscope design, two imaging systems shared the same stop that located in the distal objective. Therefore, the theoretical FOV of the OCT module is the same as

Table 1. Design indexes for video endoscope.

Object distance	15 mm
FOV	70°
Half of image height	2.71 mm
Effective focal length (EFL)	3.87 mm
f/#	7.75
Total length	230 mm
Diameter	6 mm

that of the endoscope module (70°). The axial resolution and transverse resolutions of OCT are independent of each other. The axial resolution is determined by the central wavelength and bandwidth of the light source and the lateral resolution is determined by the spot size of the beam on the sample that depends on the numerical aperture of the objective lens of the system.[14] In this paper, the RMS radii of OCT beam were set to be 15 μm and below 100 μm in the center and edge of the FOV, respectively.

3. System Design and Optimization

Figure 2 shows the flow chart of the integrated laryngoscope design:

In the design process, the system loss should also be taken into consideration. Since OCT detects back-reflected/backscattered signal and the power of laser incident on the tissue is limited due to laser safety, the elements in the common channel should be carefully selected and as few as possible.

3.1. *The design and optimization of video endoscope*

3.1.1. *Distal objective*

Usually, the distal objective of the video endoscope has short focal length, small relative aperture and large field of view angle. We selected a structure as shown in Fig. 3.[13] The structure is composed of a negative lens group $\mathbf{L}_1$ and a positive lens group $\mathbf{L}_2$ that are separated by a certain distance $\mathbf{d}$. Because the lens group $\mathbf{L}_1$ is a negative lens group, the inclination angle of the off-axis light is reduced from AOB to AOO_2 when the off-axis light passes through the lens group $\mathbf{L}_1$. As a result, a larger FOV can be achieved. In addition, since the numerical aperture of the relay system is relatively small, the distal objective should be telecentric in image space.
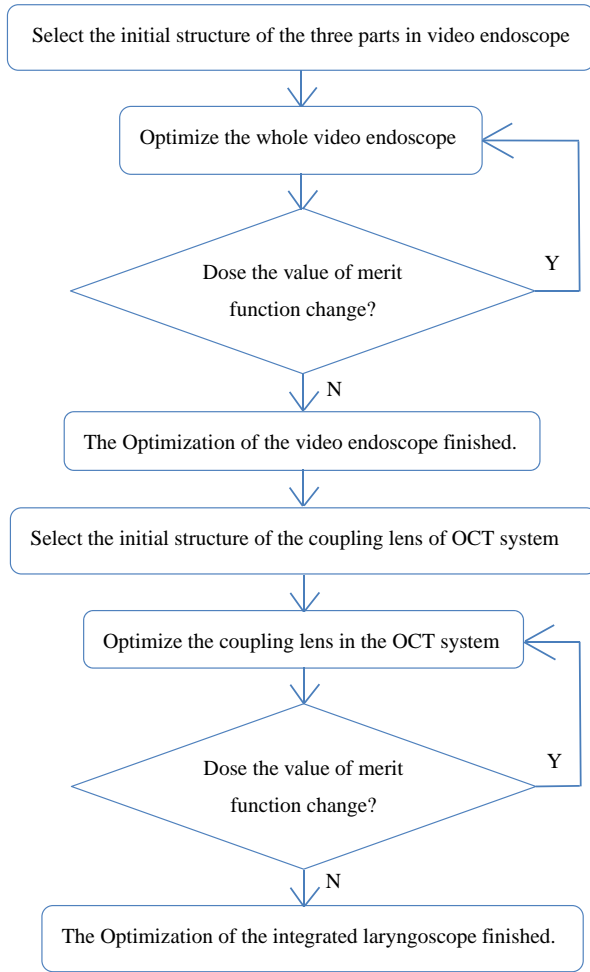
Fig. 2.   Flow chart of the integrated laryngoscope design.

Considering the power loss of the OCT system should be as small as possible, an initial four-lens structure with a similar f/# as our design in the zebase lens library was selected. The object distance, wavelength and aperture size were set according to the design requirements. The curvature, the thickness and the air space of each lens were used as variables, and the lens group optimization was carried out based on the merit function. In order to ensure that the outgoing beam from the
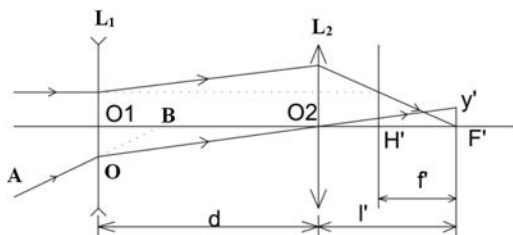
Table 2.   Lens data of the distal objective.

Surf	Type	Radius/mm	Thickness/mm	Glass
OBJ	Standard	Infinity	15	
1	Standard	Infinity	0.787	BK7
2	Standard	1.479	2.540	
STO	Standard	Infinity	0.203	
4	Standard	24.990	2.896	LAKN12
5	Standard	−3.914	1.448	
6	Standard	3.790	2.667	SK16
7	Standard	−1.899	0.813	SF4
8	Standard	−15.585	3.009	
IMA	Standard	Infinity		

objective is telecentric, operands CNAY and CNAX were added into the default merit function to limit the angle of the exit beam of each FOV. Table 2 shows the lens data of the optimized distal objective.

Figure 4 illustrates the 2D layout of the distal objective composed of a flat-concave lens, a convex lens and a doublet lens. It is shown that the FOV on the object side is about 70° and the half of the image height is 1.3 mm. Besides, the principal ray of each FOV is approximately parallel to the optical axis, that is, the system is telecentric in image space. Figure 5 shows that the resolution of the lens group is close to an ideal system since the focus spot in Fig. 5(a) and the MTF value in Fig. 5(b) at each field of view are near the diffraction limit.

3.1.2.   *Relay system*

To image the internal laryngeal tissue through oral cavity, a relay system in the laryngoscope is necessary.

Figure 6 shows three main kinds of relay system of a laryngoscope.[11] The multi-lens group structure as shown in Fig. 6(a) can provide multiple degrees of freedom for design with the aberrations well corrected. However, the power loss of OCT signal in
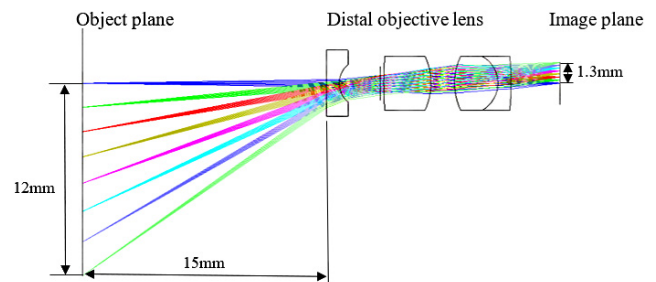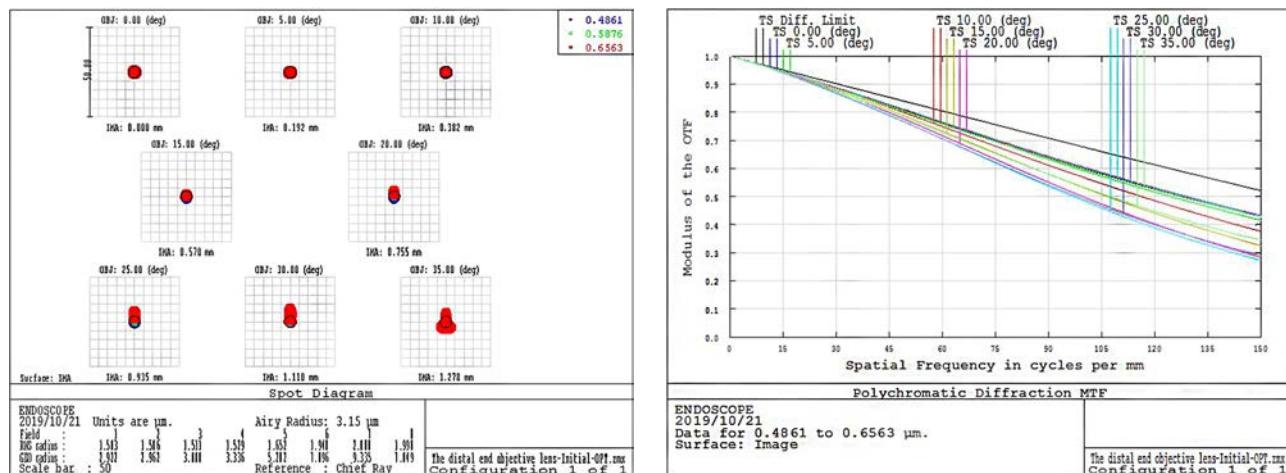

Fig. 3.   Schematic of the distal objective.

Fig. 4.   The 2D layout of the distal objective.

(a)   (b)

Fig. 5.   The spot diagram (a) and MTF (b) of the distal objective.

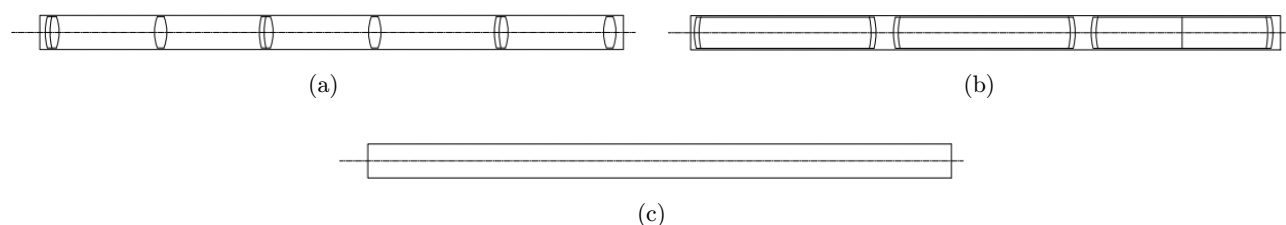(a)   (b)

(c)

Fig. 6.   Three kinds of typical relay systems: (a) Multi-lens group; (b) Hopkins rod lens; (c) GRIN lens.

an integrated system is too high using this design. Another design in Fig. 6(b) based on a rod lens known as Hopkins rod lens[15] has the advantages of relatively large aperture angle and no vertical axis aberration with a symmetrical structure, however, suffering from high power loss since multiple rod lenses are required. A GRIN lens in which the refractive index is distributed in a radial gradient[16] can also be used as a relay system.[11] Though a GRIN lens-based design has the disadvantages of a relatively small numerical aperture, chromatic aberration and field curvature,[17] the no glass-to-air gap structure ensures that the invariant of the optical system can be maximized and the light transmittance of the GRIN lens (97% at the wavelength of 1300 nm) is larger than the other two structure.[11] Moreover, the aberrations of the GRIN lens can be corrected by the overall optimization of the endoscope. Therefore, the GRIN lens-based relay system structure was chosen in our design.

Table 3 shows the lens data. The dispersion data and material properties are from the Gradient Lens Corporation (GLC) in Rochester, New York.[18]

The propagation trajectory of light with different aperture angles in a one pitch GRIN lens is shown in Fig. 7. The corresponding ray fan diagram (Fig. 8) shows that the ray fan curves of different wavelengths are relatively far apart, indicating that there is a relatively large chromatic aberration. Besides, there is an obvious field curvature since the slopes of the curves are large.

3.1.3. *Proximal objective*

As shown in Fig. 9, the image of the object imaged by the distal objective and the relay system was taken as the object **y** of the proximal objective **L**. The half image height **y**′ can be determined

Table 3.   Lens data of the GRIN lens.

Type	Radius/ mm	Thickness/ mm	Glass	Semi-diameter/ mm
Gradient6	Infinity	149	ARS31	2.35
Standard	Infinity	0.045		2.35

J. Kang et al.

Fig. 7.   Propagation trajectory of light with different aperture angles in the GRIN lens.

according to the size of CCD. Therefore, the vertical magnification of the proximal objective is given as:

$$\beta = \frac{nl'}{n'l} = \frac{y'}{y} = -2, \qquad (3)$$

where $\mathbf{n}$ and $\mathbf{n}'$ are refractive indexes of object side and image side, respectively, $\mathbf{l}$ and $\mathbf{l}'$ are object distance and image distance of the proximal objective, respectively. Because a dichroic mirror is needed to be placed between the relay system and the proximal objective, the object distance was set to be 10 mm. According to Eqs. (4) and (5), the focal length f' can be calculated to be 6.67 mm:

$$\frac{1}{l'} - \frac{1}{l} = \frac{1}{f'}, \qquad (4)$$

$$f' = -\frac{l}{1.5}. \qquad (5)$$

Since the requirement for the f/# of the proximal objective was not particularly high, we chose a symmetric structure consisting of two identical achromatic doublets. The lens data and 2D layout are shown in Table 4 and Fig. 10, respectively. The image height simulated by Zemax is the same as our theoretical values and equal to the size of CCD chip we selected. The focal length of 7.5 mm after the optimization is close to the target value of 6.67 mm. The spot and the MTF diagrams shown in Fig. 11 indicated that the resolution of the lens group in the
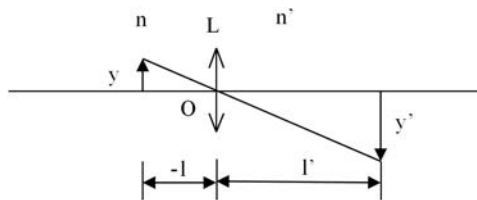

Fig. 8.   Ray fan of the GRIN lens.

Fig. 9.   Schematic diagram of Gauss formula.

center of the FOV is close to the diffraction limit. As the FOV increases, the spot size becomes larger. In the edge of the FOV, the spot size and MTF curve are gradually far from the diffraction limit. However, the resolution of the proximal objective can be improved by being put into the endoscope system for overall optimization to meet the ultimate goal.

3.1.4.   *Overall optimization of the video endoscope system*

The distal objective, the relay system and the proximal objective were all taken into consideration together for the optimization. In the optimization process, the effective focal length of the entire system was controlled by use of the operand EFFL that was added into the default merit function. The optimization initially uses the merit function based on the spot radius, and then repeatedly performed. One or more variables such as the radius of curvature of the lens, the thickness of the lens, and the air gap were selected in the repeated optimization process. It is critical to select the parameters associated with the main aberrations analyzed from the various aberration diagrams as variables to perform the optimization. When the aberrations of the system became small enough (the spot size was near the Airy radius), the merit function based on the
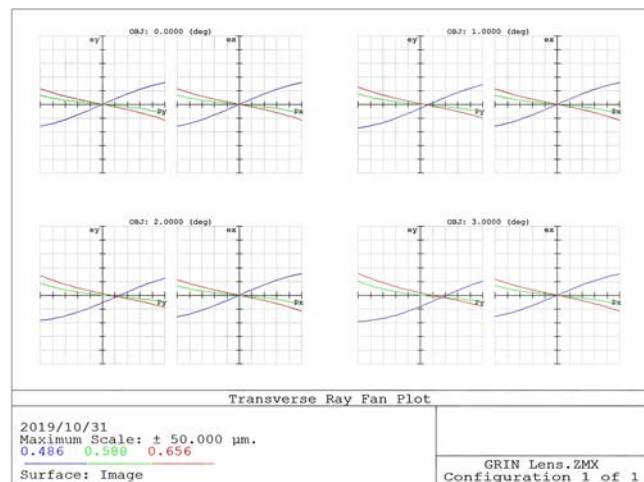
Table 4.   Lens data of the proximal objective.

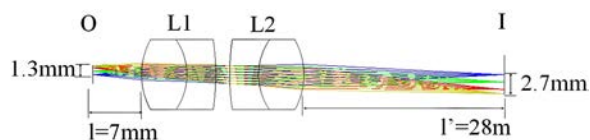| Surf	Type	Radius/mm	Thickness/mm	Glass
OBJ	Standard	Infinity	7.000	
1	Standard	10.372	6.500	H-ZBAF52
2	Standard	−8.760	4.130	H-ZF52A
3	Standard	−34.348	2.000	
4	Standard	34.348	4.130	H-ZF52A
5	Standard	8.760	6.500	H-ZBAF52
6	Standard	−10.372	28.406	
7	Standard	Infinity	—	
IMA	Standard	Infinity		

Fig. 10. The 2D layout of the original structure of the proximal objective.

wavefront was selected to continue to optimize until the value of the function was no longer changed.

The lens data and 2D layout of the optimized video endoscope system are shown in Table 5 and Fig. 12, respectively. The total length and the diameter of the system are about 230 mm and 6 mm respectively, which meet the design requirements. The image height is almost the size of the CCD chip so that the optical sensor can be fully used.

3.2. *The design and optimization of OCT system*

After the optimization of the video endoscope system, a dichroic mirror was added into the system as shown in Fig. 13 to couple the OCT sample beam into the endoscope. This configuration allows OCT signal to propagate through the same channel as the video endoscope system to minimize the size of the device. In the OCT module, the beam from a fiber collimator with a diameter of 3 mm was scanned by the 2D galvanometer, then coupled into the relay system through the coupling lens. An achromatic doublet with a focal length of 25 mm was selected as

the coupling lens based on the NA of the GRIN lens and the focus position of the OCT module. The optimization of the coupling lens was carried out based on the merit function with the initial structure as a commercial lens (Thorlabs Corporation, New York).

Table 6 illustrates the lens data of the optimized coupling lens. The 2D layout of the OCT system is shown in Fig. 13. The single-pass transmittance of the system can be over 90% since the sample arm of the OCT module is only composed of five anti-reflection coated components. Compared to other commonly-used systems with more than a dozen elements, the transmittance of the system can be significantly increased hence greatly improve the image quality and SNR of the OCT system.

4. Simulation Results and Discussions

In this section, we will discuss the image quality of the optimized video endoscopic system and the lateral resolution of the OCT system.

4.1. *Video endoscope*

Figure 14 shows the spot diagram and the MTF diagram of the endoscope system. The spot diagram indicated that the RMS radius of the spot at each FOV is less than the Airy disk radius, which means the optimized system is diffraction-constrained. Moreover, the MTF values of all FOVs are greater
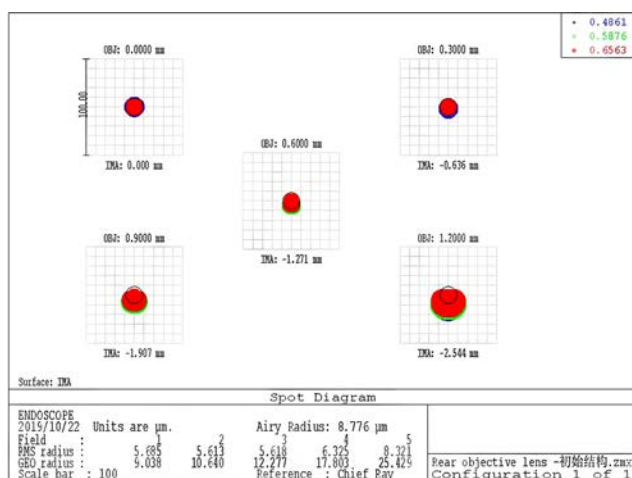
(a)
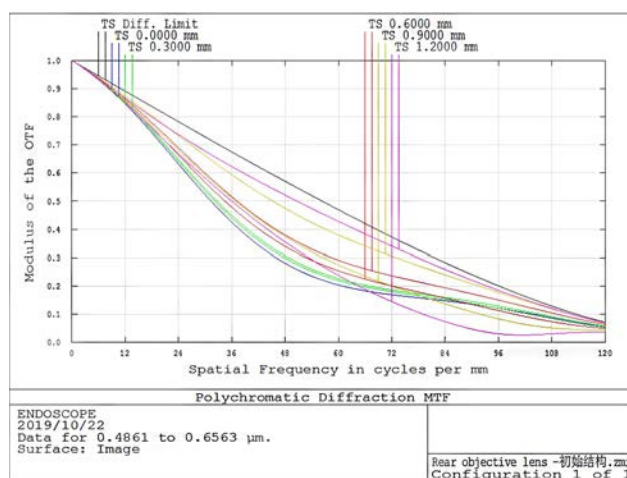
(b)

Fig. 11. The spot diagram (a) and MTF (b) of the original structure of the proximal objective.

Table 5. Lens data of video endoscope system.

| Surf	Type	Comment	Radius/mm	Thickness/mm	Glass
OBJ	Standard	Object Plane	Infinity	15	
1	Standard	Distal Objective	Infinity	2.826	BK7
2	Standard		1.217	3.803	
STO	Standard		−11.552	4.340	LAKN12
4	Standard		−5.042	2.176	
5	Standard		13.367	3.972	SK16
6	Standard		−4.359	1.132	SF4
7	Standard		−12.666	1.882	
8	Gradient6	Relay System	Infinity	149.000	ARS31
9	Standard		Infinity	25.398	
10	Standard	Proximal Objective	29.158	5.825	H-ZBAF52
11	Standard		−5.250	4.424	H-ZF52A
12	Standard		−22.497	2.151	
13	Standard		15.267	4.322	H-ZF52A
14	Standard		14.348	5.929	H-ZBAF52
15	Standard		−17.892	17.750	
16	Standard		Infinity	−0.064	
IMA	Standard	Image Plane	Infinity		
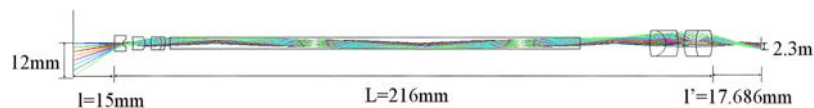
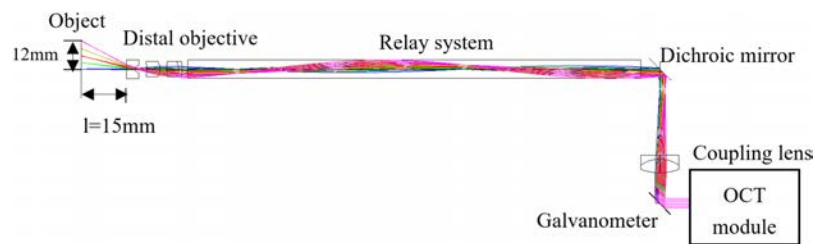Fig. 12. The 2D layout of the video endoscope system.

Fig. 13. The 2D layout of OCT system.

than 0.1 at 94 lp/mm with a cut-off frequency of 160 lp/mm, which is much higher than our design requirement.

Figure 15 shows the field curvature and the distortion of the designed video endoscopic system.

Table 6. Lens data of coupling lens for OCT.

Surf	Type	Radius/mm	Thickness/mm	Glass
1	Standard	17.704	4.519	H-ZBAF52
2	Gradient6	−10.815	1.363	H-ZF52A
3	Standard	−92.170	41.472	

The field curvature that is the distance from the image surface to the paraxial image surface is within 150 μm, resulting in little influence to image quality. In essence, distortion does not affect the resolution of the image. However, a too large distortion of the image will affect the doctors' judgment of the patient's condition. Hence, it is necessary to control the distortion of the endoscope. Compared with the relative distortion of 36% of a traditional endoscope,[19] the designed system has a much smaller relative distortion of about 20% in the maximum FOV as shown Fig. 15.
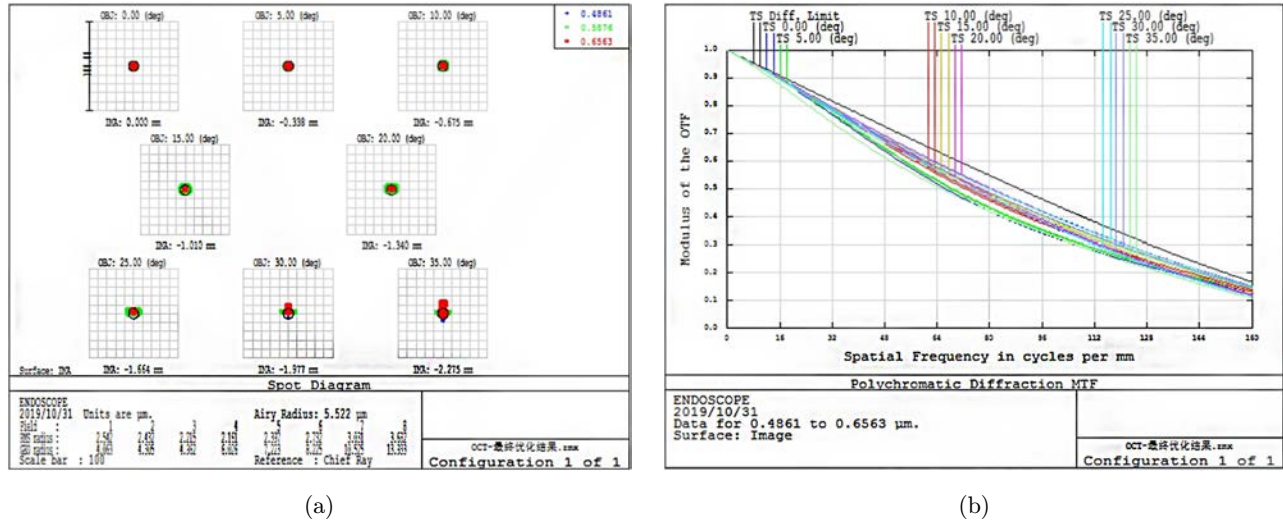
(a)   (b)

Fig. 14.   Spot diagram (a) and MTF (b) of the video endoscope system.

Figure 16 illustrated the comparison of the original image of the object (a) and the picture imaged by the endoscopic system (b), showing that the image quality of the picture imaged by the system is good without obvious chromatic aberration. The residual distortion in the edge of the FOV does not affect the clarity of the picture. In conclusion, the designed endoscope with a compact size without compromising the image quality meets the clinical requirements.

In addition, wavefront aberrations can be used to more accurately analyze the imaging quality of the system. The process of imaging the object point through the optical system can be regarded as the propagation of spherical waves through the optical system. The wavefront aberrations can be expressed as the difference between the wavefronts of the same beam passing through the actual system and an ideal system. The wavefront aberrations of the primary wavelength (0.587 nm) in different FOVs are shown in Table 7, where P–V denotes the difference of the peak to valley of the wavefront.

It can be seen that the wavefront aberration is less than $\lambda/4$ (the diffraction limit) in a FOV smaller than 25°. Although the aberrations of the object point increase with the FOV, the wavefront aberration is still near $\lambda/4$ when the FOV is greater than 25°. The analysis results of wavefront aberration is consistent with the previous image quality analysis, fully illustrating that the system is close to an ideal imaging system with a high imaging quality.

4.2.   OCT system

The lateral resolution of OCT depends on the spot size of incident beam on the sample. The lateral imaging range of the OCT module can be the same as that of the endoscope module. However, as shown in Fig. 16, there is a serious vignetting in the system when the incident beam is more than 30° off the axis. Therefore, the half of the scanning range of OCT module was set to be 30° that is 85.7% of the imaging range of the video endoscope. From Fig. 17, the RMS radii of OCT incident beam in the center and edge of the FOV are 14.948 μm and 73.609 μm, respectively, which are within and near Airy radius, respectively.
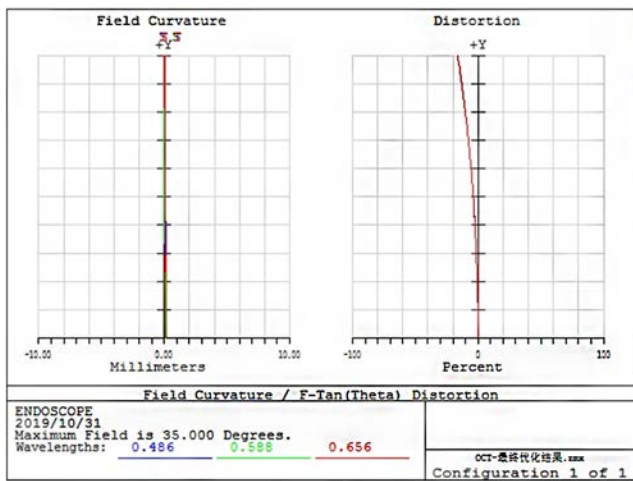

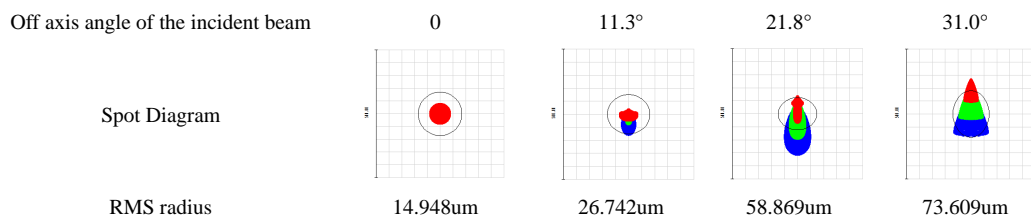Fig. 15.   Field curvature and the distortion of the video endoscope system.

J. Kang et al.

| (a) | (b) |

Fig. 16.   The simulated result of the video endoscope system. (a) The original picture of object. (b) The picture imaged by the system.

Table 7.   Wavefront aberrations of object points in different FOVs.

FOV	0°	5°	10°	15°
Wavefront Aberrations				
	P–V: 0.0569λ	P–V: 0.0688λ	P–V: 0.0569λ	P–V: 0.1053λ
FOV	20°	25°	30°	35°
Wavefront Aberrations				
	P–V: 0.2115λ	P–V: 0.2771λ	P–V: 0.3277λ	P–V: 0.3907λ

Off axis angle of the incident beam	0	11.3°	21.8°	31.0°
Spot Diagram				
RMS radius	14.948um	26.742um	58.869um	73.609um

Note: The black circle in the spot diagram represents the airy disk.

Fig. 17.   Simulated spots of OCT incident beams with different off-axis angles.

5.   Conclusion

In this paper, a design of a laryngoscope integrating OCT and video rigid endoscope is demonstrated. The system is specially optimized to reduce optical components used without compromising image quality and power loss to meet clinical demands. The integrated laryngoscope can be used to image surface and subsurface tissue of larynx simultaneously, therefore, has a potential to help physicians to make better diagnostic decisions.

Conflict of Interest

No conflicts of interest, financial or otherwise, are declared by the authors.

Acknowledgments

References

1. C. F. Sinclair, W. S. Duke, A. M. Barbu, G. W. Randolph, *Laryngeal Exam Indications and Techniques*, Springer (2016).

2. D. L. Wohl, "Nonsurgical management of pediatric vocal fold nodules," *Arch. Otolaryngol. Head Neck Surg.* **131**, 68–70 (2005).

3. D. Huang, E. A. Swanson, C. P. Lin, J. S. Schuman, W. G. Stinson, W. Chang, M. R. Hee, T. Flotte, K. Gregory, C. A. Puliafito, "Optical coherence tomography," *Science* **254**, 1178–1181 (1991).

4. N. Nassif, B. Cense, B. H. Park, S. H. Yun, T. C. Chen, B. E. Bouma, G. J. Tearney, J. F. de Boer, "In vivo human retinal imaging by ultrahigh-speed spectral domain optical coherence tomography," *Opt. Lett.* **29**, 4804–4882 (2004).

5. F. I. Feldchtein, G. V. Gelikonov, V. M. Gelikonov, R. V. Kuranov, A. M. Sergeev, N. D. Gladkova, "Endoscopic applications of optical coherence tomography," *Opt. Express* **3**(6), 257–269 (1998).

6. K. A. Vermeer, J. Van der Schoot, H. G. Lemij, J. F. De Boer, "Automated segmentation by pixel classification of retinal layers in ophthalmic OCT images," *Biomed. Opt. Express* **2**(6), 1743–1756 (2011).

7. A. M. Sergeev, V. Gelikonov, G. Gelikonov, F. I. Feldchtein, R. Kuranov, N. Gladkova, N. Shakhova, L. Snopova, A. Shakhov, I. Kuznetzova, "In vivo endoscopic OCT imaging of precancer and cancer states of human mucosa," *Opt. Express* **1**, 432–440 (1997).

8. S. Guo, R. Hutchison, R. P. Jackson, A. Kohli, T. Sharp, E. Orwin, R. Haskell, Z. Chen, B. J. Wong, "Office-based optical coherence tomographic imaging of human vocal cords," *J. Biomed. Opt.* **11**, 30501 (2006).

9. S. Guo, L. Yu, A. Sepehr, J. Perez, J. Su, J. M. Ridgway, D. Vokes, B. J. Wong, Z. Chen, "Gradient-index lens rod based probe for office-based optical coherence tomography of the human larynx," *J. Biomed. Opt.* **14**(2), 014017 (2009).

10. S. Donner, S. Bleeker, T. Ripken, M. Ptok, M. Jungheim, A. Krueger, "Automated working distance adjustment enables optical coherence tomography of the human larynx in awake patients," *J. Med. Imag.* **2**, 026003 (2015).

11. Leiner, C. Dennis, *Digital Endoscope Design* SPIE (2015).

12. J. M. Geary, *Introduction to Lens Design with Practical ZEMAX® Examples*, Willmann-Bell, Richmond (2002).

13. C. Wang, X. N. Dong, G. Cai, M. H. Chen, G. Zheng, "Design and implementation of video lens with high-definition resolution for otolaryngology endoscope," *Opt. Instrum.* **30**(3), 5–6 (2007).

14. Z. Ding, H. Ren, Y. Zhao, J. S. Nelson, Z. Chen, "High-resolution optical coherence tomography over a large depth range with an axicon lens," *Opt. Lett.* **27**, 243–245 (2002).

15. S. J. Dobson, H. H. Hopkins, "A new rod-lens relay system offering improved image quality," *J. Phys. E* **22**(7), 450–455 (1989).

16. S. Ohmi, H. Sakai, Y. Asahara, S. Nakayama, Y. Yoneda and T. Izumitani, "Gradient-index rod lens made by a double ion-exchange process," *Appl. Opt.* **27**, 496–499 (1988).

17. N. Yamamoto, K. Iga, "Evaluation of gradient-index rod lenses by imaging," *Appl. Opt.* **19**, 1101–1104 (1980).

18. Z. Manual, ZEMAX Development Corporation, WA, USA (2007).

19. Y. L. Fu, Y. Xiang, H. Wang, "Optical system design of hd wide-angle fine video rhinoscope," *J. Changchun Univ. Technol., Nat. Sci. Ed.*, **41**(01), 67–70 (2018).